where X_i is the concentration of some biogenic, nonconservative property and R_i is its regeneration rate. In order to formulate R_i, an assumption must be made concerning its depth dependence; following Suess (*17*), we set $R_i = kz_i^{-1}$ and varied k to achieve the best fit to the data (Fig. 2, C and D). This value of k was then used to find the material flux, J, across the 1500-m boundary that is required to support the changes in biogenic properties below the sill depth. This relation is integrated to the bottom. The calculated NO_3^- flux is 3.2 mmol m^{-2} $year^{-1}$, and the O_2 utilization rate is 32 mmol m^{-2} $year^{-1}$. The flux of NO_3^- or O_2 can then be related to C flux, J_C, through the Redfield stoichiometric relation: $\Delta N{:}\Delta O_2{:}\Delta C = 16{:}-138{:}106$. This approach gives two estimates for J_C: one based on O_2 consumption (0.30 g C m^{-2} $year^{-1}$) and one based on NO_3^- regeneration (0.26 g C m^{-2} $year^{-1}$). Finally, the total capture of C, integrated over the basin area (5.7×10^6 km^2), is 1.7×10^{12} g C $year^{-1}$.

Total production (PP) can be computed by application of an appropriate model to the C flux across the 1500-m boundary (Fig. 3). From the selection of models offered by Bishop (*3*) we have chosen those of Suess (*17*) [$J = PP/(0.024z + 0.21)$] and Berger *et al.* (*18*) ($J = 17\ PP/z + PP/100$), the latter of which is probably more appropriate to the deep water column. These models yield values of total PP ranging from 9 to 14 g C m^{-2} $year^{-1}$. If one uses the relation proposed by Berger *et al.* (*19*) to estimate new production ($NP = PP^2/410$), NP is about 0.5 g C m^{-2} $year^{-1}$.

It is difficult to measure PP in the Arctic Ocean directly because ice cover limits ship access and blankets coverage by remote sensing. Earlier estimates (mostly from shelves) have been based on ^{14}C uptake (*20, 21*), nutrient budgets (*22*), time-dependent chemical tracers (*23*), and the CO_2 system (*24*); they range from 1 to 45 g C m^{-2} $year^{-1}$. Our estimate, based on treating the system as a time-dependent, nutrient-regenerating water mass falls at the low end of this range; it represents a millennium-long average, well suited as a backdrop for comparison of shorter term fluctuations. It must be considered a minimum, however, because we have ignored in the calculation material that becomes permanently preserved in the sediment, a fraction generally presumed to be small. For example, Berger *et al.* (*18, 19*) suggested that most of the organic C arriving at the sea floor is consumed near the interface; perhaps only 10% of what reaches the deep ocean sediments is permanently preserved. Although the empirical models used here were developed in temperate oceans, data from the Antarctic suggest they may also be used in ice-covered seas (*25*). Clearly, to verify this approach, we need to develop better models of particle flux and C regeneration applied specifically to polar environments on the basis of time series data from sequential sediment traps. Other questions remain: what controls the resupply of NO_3^- to surface water, and how much of the deep C flux derives from shelf and slope regions?

REFERENCES AND NOTES

1. R. C. Dugdale and J. J. Goering, *Limnol. Oceanogr.* **23**, 196 (1967).
2. R. W. Epply and B. J. Peterson, *Nature* **282**, 677 (1979).
3. J. K. B. Bishop, in *Productivity of the Ocean: Past and Present*, W. H. Berger, V. S. Smetacek, G. Wefer, Eds. (Wiley, Chichester, 1989), pp. 117–137.
4. H. G. Ostlund, G. Possnert, J. H. Swift, *J. Geophys. Res.* **92**, 3769 (1987).
5. K. Aagaard, *Deep-Sea Res.* **28**, 251 (1981).
6. J. H. Swift and K. P. Koltermann [*J. Geophys. Res.* **93**, 3563 (1988)] discussed salinity variability within the deep waters of the Arctic-Mediterranean system.
7. E. C. Carmack, in *Polar Oceanography*, part A, *Physical Science*, W. O. Smith, Ed. (Academic Press, San Diego, 1990), pp. 171–222; $\delta^{18}O = [(^{18}O/^{16}O_{sample} - ^{18}O/^{8}O_{SMOW})/(^{18}O/^{16}O_{SMOW})] \cdot 10^3$, where SMOW is standard mean ocean water.
8. W. G. Metcalf, *Deep-Sea Res.* 7, 190 (1960).
9. K. Aagaard, J. H. Swift, E. C. Carmack, *J. Geophys. Res.* **90**, 4833 (1985).
10. C. Wilson and D. W. R. Wallace, *ibid.* **95**, 22193 (1990).
11. F. Bryan [*Nature* **323**, 301 (1986)] introduced the notion that long-term fluctuations in deep-water salinity can influence the thermohaline circulation.
12. R. W. Macdonald *et al.*, *Can. Data Rep. Hydrogr. Ocean Sci.* 80 (1990).
13. R. P. Beukens, D. M. Gurfinkel, H. W. Lee, *Radiocarbon* **28**, 229 (1986).
14. The deep water (<1250 m) in the Canada Basin was also sampled at T3 [P. Kinney *et al.*, *J. Geophys. Res.* **75**, 4097 (1973)], LOREX [R. M. Moore *et al.*, *ibid.* **88**, 2667 (1983)], and AIWEX (J. H. Swift, personal communication).
15. M. Scranton *et al.*, *Deep-Sea Res.* **34**, 945 (1987).
16. The model used here follows that of Scranton *et al.* (*15*). Integrations were carried out over the depth range of 1400 to 4000 m with 100-m depth intervals, and time steps of 1 year. Initial conditions were chosen from present-day values at sill depth; for example ^{14}C age = 60 years, $NO_3^- = 13.3$ mmol m^{-3}, and $O_2 = 309$ mmol m^{-3}. We applied hypsographic corrections, using Aagaard *et al.* (*9*).
17. E. Suess, *Nature* **288**, 260 (1980).
18. W. H. Berger *et al.*, in *Biogeochemical Cycling and Fluxes Between the Deep Euphotic Zone and Other Oceanic Realms*, C. Agegian, Ed. (National Oceanic and Atmospheric Administration Symposium Series for Undersea Research, U.S. Department of Commerce, Washington, DC, 1987), pp. 131–176.
19. W. H. Berger, V. S. Smetacek, G. Wefer, in *Productivity of the Ocean: Past and Present*, W. H. Berger, V. S. Smetacek, G. Wefer, Eds. (Wiley, Chichester, 1989), pp. 1–34.
20. D. V. Subba-Rao and T. Platt, *Polar Biol.* **3**, 191 (1984).
21. T. S. English, *Arctic Inst. North Am. Res. Pap.* 13 (1961).
22. R. W. Macdonald, C. S. Wong, P. Erickson, *J. Geophys. Res.* **92**, 2939 (1987).
23. D. W. R. Wallace, R. M. Moore, E. P. Jones, *Deep-Sea Res.* **34**, 1957 (1987).
24. L. Anderson, D. Dyrssen, E. P. Jones, *J. Geophys. Res.* **95**, 1703 (1990).
25. G. Wefer, G. Fischer, D. Fuetterer, R. Gersonde, *Deep-Sea Res.* **35**, 891 (1988).
26. We thank E. P. Jones, K. Aagaard, and two anonymous reviewers for helpful comments. In particular, we thank Captain D. Johns and I. Cote of Coast Guard Northern for their continuing efforts to provide oceanographic platforms, and Captain D. S. McGarvie, the officers, and crew of C.C.G.S. *Sir John Franklin*. Nutrient and O_2 determinations were provided by F. McLaughlin and M. O'Brien. This work was jointly supported by Fisheries and Oceans Canada and Indian and Northern Affairs Canada under Northern Oil and Gas Action Program B.6.

6 June 1991; accepted 13 August 1991

Orientational Disorder in Solvent-Free Solid C_{70}

GAVIN B. M. VAUGHAN, PAUL A. HEINEY,* JOHN E. FISCHER,
DAVID E. LUZZI, DEBORAH A. RICKETTS-FOOT, ANDREW R. MCGHIE,
YIU-WING HUI, ALLAN L. SMITH, DAVID E. COX,
WILLIAM J. ROMANOW, BRENT H. ALLEN, NICOLE COUSTEL,
JOHN P. MCCAULEY, JR., AMOS B. SMITH III

The high-temperature structure of solvent-free C_{70} has been determined with high-resolution x-ray powder diffraction and electron microscopy. Samples crystallized from solution form hexagonal close-packed crystals that retain an appreciable amount of residual toluene, even after prolonged heating. Samples prepared by sublimation, which contain no detectable solvent, are primarily face-centered cubic with some admixture of a hexagonal phase. The relative volume of the hexagonal phase can be further reduced by annealing. The structures of both phases are described by a model of complete orientational disorder. The cubic phase contains an appreciable density of stacking faults along the [111] direction.

SOLID C_{60} IS A VAN DER WAALS-bonded molecular crystal (*1*) which exhibits an orientational ordering transition at $T_c = 249$ K (*2*). Both high- and low-temperature structures are characteristic of cubic close-packed pseudospheres, consistent with the molecular geometry (*3*). At high temperature (T), all molecules are crystallographically equivalent due to dynamic orientational disorder (*4*), while at low temperature the dynamics are frozen out to yield a simple cubic structure with *Pa3* symmetry, thus breaking the orientational equivalence (*2, 5–8*). The next-larger fullerene, C_{70}, is of lower D_{5h} symmetry (*9*) (Fig. 1, inset). Its elongated "rugby-ball" shape should inhibit free rotations, thus increasing T_c. The reduced symmetry also suggests possible intermediate phases with partial orientational order (for example, disorder about the long axis only, or long axes aligned along specific crystal directions).

Fleming *et al.* reported that C_{70} co-crystallized with pentane is monoclinic (*10*), and suggested that sublimed C_{70} at 300 K has the same structure as C_{60}, that is, a face-centered cubic (fcc) Bravais lattice with complete orientational disorder (*11*). Nuclear magnetic resonance (NMR) shows that the disorder is dynamic at 300 K (*4*). We report here a detailed study of C_{70} that made use of x-ray diffraction (XRD), transmission electron microscopy (TEM), differential scanning calorimetry (DSC), and diffuse reflectance infrared spectroscopy (IR). Structural transitions are indeed observed in the XRD and DSC data, but the low-T phase (or phases) are still incompletely characterized. Thus the focus of this paper is on the high-symmetry structure observed at and above 300 K, and the considerable efforts required to produce samples from which this information could be reliably obtained.

C_{70} was prepared as described elsewhere for C_{60} (*1*), except that repeated chromatography was required to obtain >99% purity. Extraction of soluble fullerenes from soot was done with cold toluene, and the chromatography was followed by a hexane wash and vacuum-drying (10^{-2} torr) at 525 K for 12 to 18 hours. In the case of C_{60}, this procedure yields highly crystalline material with a low density of stacking faults, no residual solvent detectable by IR, and a single DSC endotherm at T_c (*12*), but not in the case of C_{70}, as discussed below. X-ray samples of C_{70} consisted of 1 to 2 mg powder, sealed into quartz capillaries under an inert atmosphere. These were mounted in either a closed-cycle helium refrigerator or a small cylindrical heater for measurements below and above 300 K respectively. X-ray patterns were collected at beamline X7A at the Brookhaven National Synchrotron Light Source (NSLS) (*13*).

A 440 K pattern of C_{70} prepared as described above is shown in Fig. 1a. All peaks can be indexed on a hexagonal cell with a = 10.63 Å and c = 17.39 Å. The full widths at half-maximum (FWHM) are typically 0.015 $Å^{-1}$. Hexagonal close-packing (hcp) is suggested by systematic absences and the 1700 $Å^3$ volume of a two-molecule cell. TEM measurements on samples prepared by filtering powder suspended in ethanol onto grids also indicate a hexagonal lattice, but the crystals were unstable under the condensed 120-keV beam; the contrast changed rapidly with time, and we observed bubbling of surface films and a reduction in the volume of crystalline material. Similar effects occur in solvent-containing C_{60}/C_{70} mixtures (*14*). The infrared spectrum of this sample (*15*) revealed bands at 694 cm^{-1} and 724 cm^{-1} attributable to the strongest absorptions of toluene, and additional bands between 1416 cm^{-1} and 1566 cm^{-1} consistent with C=C stretching modes of the benzene ring in toluene (*16*), as well as the previously identified C_{70} bands (*17*). In contrast, no known bands due to hexane (*18*) were observed. DSC combined with mass spectrometry showed sharp endotherms in the range 395 to 445 K, which we attribute to decomposition of a toluene-C_{70} complex. These were not observed upon reheating in an open pan but persisted after cycling in a sealed pan, indicating that toluene leaves and reenters the sample upon temperature cycling. The IR and DSC results indicate that neither the hexane wash nor the subsequent vacuum-drying procedure is sufficient to remove all the toluene from C_{70}.

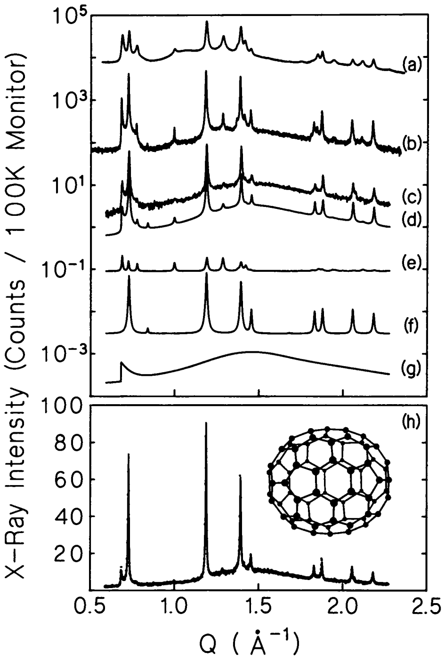

Fig. 1. X-ray powder diffraction patterns from C_{70} samples, and results of least-squares fits. All curves except for c are offset for clarity. Typically, 100 K monitor counts corresponds to approximately 5 seconds. Abscissa units $q = (4\pi/\lambda)\sin\theta = 2\pi/d$. Curve a: XRD powder pattern from solvated C_{70} sample, measured at 440 K. Curve b: Pattern of sublimed sample at 440 K. Curve c: Pattern of sublimed-annealed sample at 325 K. Curve d: Result of least-squares model fit to pattern (curve c) assuming fcc-hcp coexistence with spherically averaged molecules, as discussed in text. Curve e: Portion of fit (curve d) due to the model hcp structure. Curve f: Portion of fit (curve d) due to the model fcc structure. Curve g: Portion of fit (curve d) due to model background scattering, including the sawtooth lineshape at 0.678 $Å^{-1}$. Curve h: Linear plot of curves c and d. Points are data; the solid line is the result of the least-squares fit. Inset: structure of the C_{70} molecule (*22*).

An improved sample was prepared by subliming ~30 mg of vacuum-dried C_{70} powder in a dynamically pumped quartz tube with the C_{70} source at 810 K for 12 hours. Solid C_{70} condensed only near the furnace exit, where the quartz temperature was near 300 K. Amorphous holey carbon grids were placed near the cool end to prepare witness TEM samples. After slow cooling, ~12 mg of C_{70} powder were collected. The IR spectrum showed no bands attributable to either solvent. We conservatively estimate a 0.1% upper limit on the toluene mass (*19*). The 440 K XRD pattern from this sample, Fig. 1, curve b, is qualitatively similar to that of Fig. 1, curve a, except that the peaks are sharper (typically 0.005 $Å^{-1}$ FWHM) and the relative intensities differ. Most peaks can be indexed both as hcp (a = 10.62 Å, c = 17.31 Å) and as fcc (a = 15.01 Å). Exceptions are the uniquely indexed peaks such as the fcc 200 at 0.837 $Å^{-1}$ and the hcp 102 at 0.936 $Å^{-1}$. The observation of both sets of uniquely indexed peaks is clear evidence that this spectrum must be interpreted as a mixture of the two structures (*20*). From least-squares fits to a mixed-phase mod-

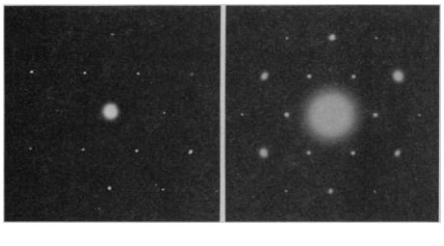

Fig. 2. (**Left**) fcc [110] zone axis electron diffraction pattern of sublimed C_{70}. The reflections aligned vertically are $\bar{2}20$-type with the 002 reflections (horizontal), weak due to form factor effects. The 4 reflections closest to the origin are $\bar{1}11$-type. (**Right**) fcc [111] zone axis pattern. The expected 6 fcc $\bar{2}20$-type reflections lie on the vertical and at ±60° from the vertical. The 6 reflections closest to the transmitted beam are due to rods of scattering aligned along [111]. In this pattern the effective Miller indices are $\{\bar{2}/3, \bar{2}/3, 4/3\}$.

G. B. M. Vaughan, P. A. Heiney, B. H. Allen, Laboratory for Research on the Structure of Matter and Physics Department, University of Pennsylvania, Philadelphia, PA 19104.
J. E. Fischer, D. E. Luzzi, N. Coustel, Laboratory for Research on the Structure of Matter and Materials Science and Engineering Department, University of Pennsylvania, Philadelphia, PA 19104.
D. A. Ricketts-Foot, A. R. McGhie, W. J. Romanow, Laboratory for Research on the Structure of Matter, University of Pennsylvania, Philadelphia, PA 19104.
Y. W. Hui and A. L. Smith, Chemistry Department, Drexel University, Philadelphia, PA 19104.
D. E. Cox, Physics Department, Brookhaven National Laboratory, Upton, NY 11973.
J. P. McCauley, Jr., and A. B. Smith III, Laboratory for Research on the Structure of Matter and Chemistry Department, University of Pennsylvania, Philadelphia, PA 19104.

---

*To whom correspondence should be addressed.

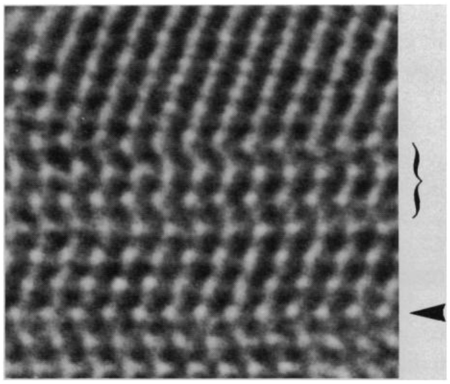

Fig. 3. [110] zone axis TEM image of fcc C_{70}. Each white feature corresponds to a column of C_{70} molecules lying parallel to the electron beam. The ($\bar{1}$11) planes [or (0001) in hcp] are viewed edge-on horizontally. The curly bracket indicates an hcp-type stacking fault, and the arrow denotes an fcc twin plane.

el incorporating orientational disorder (discussed below), we estimate that ~21 vol.% of this sample is hcp at 440 K.

Bright field TEM images from the witness grids revealed small grains of predominantly fcc C_{70} which were stable under the 120 keV electron beam. This provides further evidence that sublimation largely eliminated the problem of toluene retention. The sharp [110] zone axis patterns (Fig. 2, left) contain two sets of $\bar{1}$11 reflections at 70.5°, as well as a $\bar{2}$20 reflection at 35.3° from each $\bar{1}$11 and a faint 002 reflection at 90° from the $\bar{2}$20. These are all characteristics of fcc diffraction. The threefold [111] zone axis pattern (Fig. 2, right) exhibits strong $\{\bar{2}\ 2\ 0\}$ reflections at $q = 1.19$ Å^{-1}. Three additional sets of non-fcc reflections along the $\langle\bar{2}\bar{2}4\rangle$ directions, at a smaller spatial frequency $q = 0.69$ Å^{-1}, correspond to a Miller index $\{\bar{2}/3, \bar{2}/3, 4/3\}$. When the specimen was tilted about a [$\bar{2}$20]-type tilt axis, these extra reflections did not disappear but moved in q, ultimately reaching the positions of the $\bar{1}$11 reflections in the [110] zone axis pattern. These low-q features thus result from rods of intensity along a single fcc [111] crystallographic direction, arising from hcp stacking faults, as previously observed in sublimed C_{60} (*21*). High-resolution TEM images showed predominantly large fcc regions. The [110] zone axis image in Fig. 3 shows typical defect structures. In the top part of the image, the stacking of close-packed layers is ABCABC, that is, unfaulted fcc. The curly bracket indicates four close-packed layers with ABAB stacking, that is, an hcp-type fault. The arrow indicates an fcc twin plane ABCBA sequence. Overall, the faults occur in clusters rather than being uniformly distributed throughout the grains.

In an effort to prepare a single-phase sample, C_{70} powder prepared by sublimation as discussed above was annealed for 200 hours at 575 K in a sealed capillary. The powder XRD pattern from this sample (Fig. 1, curve c) must still be indexed as a mixture of fcc and hcp phases, but the relative amount of hcp has decreased markedly. The peak widths have also increased by a factor of 2. Similar in situ annealing of the TEM sample revealed a reduction in rod intensity indicating partial removal of isolated hcp faults.

Figure 1, curve d, shows the result of a least-squares fit to the diffraction pattern of Fig. 1, curve c, carried out with the following model. All peaks were well described by Lorentzian line shapes

$$I(q) = [I(G)/2\pi\kappa]/\left[\frac{q - G}{\kappa} + \frac{1}{4}\right]$$

with the full width κ intrinsic rather than instrumentally limited, and of the form $\kappa = \alpha + \beta\sin\theta$. We further assumed that the C_{70} molecules were orientationally disordered in coexisting hcp and fcc phases. For C_{60}, the x-ray form factor of a freely rotating molecule is given (*1, 2*) by $f_{\text{mol}}(q) = 60f_c(q)\sin(qR)/(qR)$ where f_c is the carbon atom form factor and R the molecular radius. In C_{70}, there are several C atoms at different radii, and the molecular form factor becomes

$$f_{\text{mol}}(q) = f_c(q)\sum_{i=1}^{70}\frac{\sin(qR_i)}{qR_i} \qquad (1)$$

We used atomic coordinates calculated by Baker *et al.* (*22*). There are 10 atoms at a radius of 4.173 Å, 10 at 4.029 Å, 20 at 3.876 Å, 20 at 3.663 Å, and 10 at 3.565 Å. Within each phase, the integrated scattering intensity at reciprocal lattice vector G is described by

$$I(G) = I_0 LP f_{\text{mol}}{}^2 M\, F_{\text{lat}}{}^2\,\frac{1}{V^2} \qquad (2)$$

Here I_0 is a constant multiplicative prefactor, LP is the Lorentz-polarization factor appropriate to the scattering geometry at NSLS X7A, M is the multiplicity of peak G, F_{lat} is the lattice structure factor (equal to 0 or 4 for fcc, and 0, 1, $\sqrt{3}$, or 2 for hcp), and V is the unit cell volume.

The smooth background present at all wave vectors, and the broad feature near 1.5 Å^{-1}, result primarily from scattering from the capillary and air, and could be parametrized by a quadratic function plus two broad Gaussian peaks. The sharp feature at 0.678 Å^{-1} can be indexed as the 100 peak of the hcp phase. However, as discussed above this feature arises at least in part from stacking-fault-induced Bragg rods in reciprocal space; in a powder diffraction scan, such rods result in a sawtooth lineshape (*21, 23*). Therefore, in addition to the Lorentzian hcp Bragg peak at this position, we added a simple sawtooth lineshape with adjustable amplitude I_s and width δ:

$$I_{\text{saw}}(q) = \begin{cases} 0 & \text{if } q < q_0 \\ I_s\exp\{[\cos^{-1}(q_0/q)/\delta]^2\} & \text{if } q \geq q_0 \end{cases} \qquad (3)$$

The fit shown in Fig. 1, curve d, clearly reproduces the important features of the spectrum, although it is not perfect; the goodness-of-fit parameter χ^2 is 2.8. The fcc amplitude parameter is 7.6 times the hcp amplitude parameter, demonstrating that 11 ± 3% of the molecules are in the hcp phase. The fitted lattice constant of $a = 14.96$ Å for the fcc phase is very close to $\sqrt{2}$ times the hexagonal "a" of 10.56 Å, while the hexagonal $c = 17.35$ Å yields a $c{:}a$ ratio of 1.64, very close to the ideal close-packed ratio of 1.63. These lattice parameters are all marginally smaller than those measured for the solvent-prepared and unannealed sublimed samples.

For the fcc phase, the peak width is described by $\kappa = (0.0050 + 0.017\sin\theta)$Å^{-1} while for the hcp phase it is given by $\kappa = (0.092\sin\theta)$Å^{-1}. This implies that in the fcc phase the limiting crystallite size is on the order of $2\pi/\kappa = 1250$ Å, but strains and related defects ("paracrystalline disorder") also make an important contribution to the broadening. In the hcp phase the paracrystalline disorder is stronger, but the error bars on these parameters are larger due to the relatively low intensity of the pure hcp peaks. Compared to the unannealed sublimed sample, the sawtooth amplitude is 5 to 10 times smaller relative to the fcc intensity, indicating a dramatic reduction in stacking fault density, consistent with TEM.

All samples studied exhibited a transition to a low-temperature phase (or mixture of phases) whose structure has not yet been determined. DSC measurements on sublimed samples showed only two reproducible transitions with onsets at 276 K and 337 K and heats of transition of 3.5 ± 0.5 and 2.7 ± 0.3 J g^{-1}. The combined value of 6.2 J g^{-1} is similar to the heat of the orientational transition observed in C_{60} (*2*). Using XRD, we generally observed coexistence between the high-temperature hcp and/or fcc phases with a characteristic low-temperature pattern over a range between 240 K and 325 K (*24*), with a 25 K to 50 K hysteresis in the transition temperature.

The observations of a nearly perfect $c{:}a$ ratio in the hexagonal phase and of fcc ordering naturally imply that approximately spherical objects, such as orientationally disordered molecules, are being packed into the lattice at high T. Indeed, if the molecules are not orientationally disordered, it is hard to reconcile the high symmetry of the lattice with the relatively low D_{5h} symmetry of the molecule (*9*). However, the molecules are not necessarily sampling all spherically symmetric orientations. It is possible, for example, that in the fcc phase the long axes of the molecules randomly sample the different ⟨111⟩ directions.

Our data indicate that the fcc phase is the equilibrium state of pure C_{70} above 300 K. However, the hcp phase is energetically similar to the fcc phase, and can most likely be nucleated by a number of effects, including solvent, powder-grain surfaces, crystal domain boundaries, and so forth. The fraction of hcp phase can thus be reduced by solvent removal, but further reduction requires prolonged thermal annealing, as observed.

REFERENCES AND NOTES

1. J. E. Fischer *et al.*, *Science* **252**, 1288 (1991).
2. P. A. Heiney *et al.*, *Phys. Rev. Lett.* **66**, 2911 (1991).
3. H. W. Kroto *et al.*, *Nature* **318**, 162 (1985).
4. R. Tycko *et al.*, *J. Phys. Chem.* **95**, 518 (1991).
5. W. I. F. David *et al.*, *Nature* **353**, 147 (1991).
6. R. Sachidanandam and A. B. Harris, *Phys. Rev. Lett.* **67**, 1468 (1991).
7. S. Liu, Y-j. Lu, M. M. Kappes, J. A. Ibers, *Science* **254**, 408 (1991).
8. J. R. D. Copley *et al.*, *Physica B*, in press.
9. R. Taylor *et al.*, *J. Chem. Soc. Chem. Comm.* **20**, 1423 (1990).
10. R. M. Fleming *et al.*, *Phys. Rev.* **B44**, 888 (1991).
11. R. M. Fleming, in *Large Carbon Clusters*, American Chemical Society Symposium Series, in press.
12. J. E. Fischer, P. A. Heiney, D. E. Luzzi, D. E. Cox, in *ibid.* (in press).
13. For the powder XRD measurement on the solvent-prepared sample, the experimental configuration at beamline X7A consisted of a Si(111) channel-cut monochromator set for a wavelength of 1.5435 Å, an ion-chamber to monitor the incident beam intensity, and a 1 mm receiving-slit in front of a Peltier-cooled semiconductor detector. The measurements on the sublimed sample employed a wavelength of 1.2987 Å, and a Ge(220) analyzing crystal was placed before the detector to improve the instrumental resolution and enhance the signal-to-background ratio. For measurements on the annealed sublimed sample, a Ge(111) channel-cut monochromator and Ge(220) analyzing crystal were employed, with a wavelength of 1.2981 Å.
14. G. Van Tendeloo *et al.*, *Europhys. Lett.* **15**, 295 (1991).
15. With the use of a Perkin-Elmer 1600 FTIR with a diffuse reflectance attachment, approximately 0.5 mg of C_{70} was placed on a layer of KBr powder on the sample tray. Five hundred scans at 2 cm^{-1} resolution, referenced against the KBr powder itself, were summed. Bands were seen at 504, 534, 564, 578, 642, 674, 794, 1134, and 1430 ± 1 cm^{-1}.
16. Sadtler Research Labs, Standard IR Spectra, No. 419, Philadelphia, PA (1962).
17. D. S. Bethune *et al.*, *Chem. Phys. Lett.* **179**, 181 (1991).
18. Sadtler Research Labs, No. 678, see (*16*).
19. Our estimate of a 0.1% upper limit on the toluene mass can be justified as follows: TGA analysis of vacuum-dried samples shows a weight loss of 3 to 5% in the range 395 to 444 K due to toluene evolution. By comparing the area under the 694 and 724 cm^{-1} IR toluene peaks, we estimate that the sublimed sample has 50 times less toluene than the vacuum-dried sample. The diffuse IR reflectance measurement actually provides the most sensitive measurement of the amount of residual solvent in the sample, since the NMR limit of detectability of residual impurities is generally also in the 0.1% range and often closer to 1 to 2%.
20. Note that the fcc-only peaks are sufficiently weak that they would not have been observed in the spectrum of the solvent-prepared sample, which had a much higher relative level of diffuse scattering.
21. D. E. Luzzi *et al.*, *J. Mat. Res.*, in press.
22. J. Baker *et al.*, *Chem. Phys. Lett.* **184**, 182 (1991).
23. B. E. Warren, *Phys. Rev.* **59**, 693 (1941).
24. We note, therefore, that diffraction patterns collected from such samples at room temperature will generally contain peaks from two or more phases, depending on the thermal history of the sample.
25. We thank A. Denenstein, N. C. Maliszewskyj, P. Sprengler, O. Zhou, and Q. Zhu for their technical assistance, and A. Cheng for useful discussions. This work was supported by the National Science Foundation, under Grants DMR-88-19885 and DMR-89-01219, and by the Department of Energy, DE-FC02-86ER45254 and DE-FG05-90ER75596. The work at Brookhaven was also supported by DOE, Division of Materials Sciences, DEAC02-76CH00016.

3 October 1991; accepted 30 October 1991

Computer Simulations of Self-Assembled Membranes

J.-M. DROUFFE, A. C. MAGGS, S. LEIBLER*

Molecular dynamics simulations in three dimensions of particles that self-assemble to form two-dimensional, membrane-like objects are presented. Anisotropic, multibody forces, chosen so as to mimic real interactions between amphiphilic molecules, generate a finite rigidity and compressibility of the assembled membranes, as well as a finite line tension at their free edges. This model and its generalizations can be used to study a large class of phenomena taking place in fluctuating membranes. For instance, both fluid and solid-like phases, separated by a phase transition, are obtained and some of the large-scale properties of these membranes studied. In particular, thermal undulations of quasi-spherical fluid vesicles are analyzed, in a manner similar to recent experiments in lipid systems.

AMPHIPHILIC MOLECULES THAT ARE brought into contact with water tend to assemble so as to orient their polar hydrophilic "heads" toward the water and their oily hydrophobic "tails" away from it. Among the simplest structures formed in this way are bilayer membranes, whose lateral dimensions can largely exceed their typical thicknesses (*1*). Such (quasi–)two-dimensional molecular assemblies can then form a large variety of thermodynamic phases: closed vesicles, lamellar or cubic crystals, and disordered bicontinuous networks (*2*). Despite definite progress made recently in experimental and theoretical studies of the physical properties of membranes and of the process of their self-assembling (*3*), many aspects of these structures still remain poorly understood. From the theoretical point of view, available analytical and numerical methods are largely insufficient to solve models based on realistic microscopic interactions between amphiphilic molecules surrounded by water. For instance, numerical simulations of truly microscopic models are only possible for very small aggregates such as micelles (*4*). The time scales involved in the largest molecular simulations are much too short to describe the formation and the thermodynamic behavior of larger assemblies such as membranes.

This situation has led to the development of phenomenological theories in which membranes are treated as fluctuating surfaces, described by an effective elastic (free) energy functional, $\mathcal{F}$ (*1*). The effective energy depends on details of shape (such as curvature) (*5*) and topology of the membrane, but it can also take into account additional internal degrees of freedom of its molecular components describing membrane fluidity, chirality, and so forth. Starting with appropriate effective functionals $\mathcal{F}$, one can build thermodynamic models of various types of fluctuating membranes: fluid (*5*), hexatic (*6, 7*), solid-like or polymerized (*6*), with different topologies (*8*) and effective interactions. Because universal properties of the fluctuating membranes (such as the spectrum of their large-scale excitations or the critical indices of various phase transitions involving membranes) should not depend on microscopic details, studying these phenomenological models can yield useful predictions about real systems (*9*).

In this report we describe another approach to the computer simulations of fluctuating membranes. It is similar in spirit to the approach used in many recent numerical studies of solid-like (*10*) and fluid (*11, 12*) membranes in that it does not start with realistic microscopic interactions and thus concentrates only on the universal, large-scale properties of simulated systems. However, in contrast to the previous simulations which start with some kind of a triangulated surface [such as a "tethered" network of impenetrable spheres (*13*) or a surface with fluctuating triangulation (*11*)], the mem-

---

J.-M. Drouffe and S. Leibler, Service de Physique Théorique de Saclay, F-91191 Gif-sur-Yvette Cedex, France.
A. C. Maggs, Laboratoire de Physico-Chimie Théorique, Ecole Supérieure de Physique et de Chimie Industrielles, F-75231 Paris Cedex 05, France.

*To whom correspondence should be addressed.